Two-dimensional Navier–Stokes simulations of gaseous mixtures induced by Richtmyer–Meshkov instability

Claude Mügler and Serge Gauthier

Citation: Phys. Fluids **12**, 1783 (2000); doi: 10.1063/1.870427
View online: http://dx.doi.org/10.1063/1.870427
View Table of Contents: http://pof.aip.org/resource/1/PHFLE6/v12/i7
Published by the American Institute of Physics.

Two-dimensional Navier–Stokes simulations of gaseous mixtures induced by Richtmyer–Meshkov instability

Claude Mügler[a)] and Serge Gauthier
Commissariat à l'Énergie Atomique/Bruyères-le-Châtel, Boîte Postale 12, 91680 Bruyères-le-Châtel, France

(Received 23 June 1999; accepted 3 April 2000)

Two-dimensional numerical calculations of the fluid instability of shock-accelerated interfaces between a heavy fluid and a light one are carried out in order to simulate experiments performed by Poggi *et al.* [Phys. Fluids **10**, 2698 (1998)]. In these experiments, the laser Doppler anemometry technique gives measurements of the fluctuating velocity. Experimental data show that a turbulent mixing zone is generated by the incident shock wave. This turbulent regime is reproduced by two-dimensional calculations. Before the first reshock, several quantities in the mixing zone, such as bubble and spike fronts, turbulent kinetic energy, enstrophy, adopt a quasi self-similar behavior versus time. In particular, we can see in numerical simulations the decay of the turbulent kinetic energy before the first reflected shock wave–mixing-zone interaction and its strong enhancement by reshocks. Furthermore, spectral analysis of the numerical results exhibit a k^{-3} energy spectrum. Experimental measurements also show that the turbulent boundary layers which develop on the shock-tube walls accelerate the fluid flow in the middle of the tube. Numerical simulations clearly reproduce both this acceleration and the lambda-shock structure observed in experiments. © *2000 American Institute of Physics.* [S1070-6631(00)01207-1]

I. INTRODUCTION

When two different fluids are impulsively accelerated into each other by a shock wave, small perturbations at the interface grow first linearly and then evolve into nonlinear structures having the form of ''bubbles'' and ''spikes.'' Afterwards, it may lead to the formation of a turbulent mixing zone. This instability was theoretically discovered and described by Richtmyer,[1] and experimentally confirmed by Meshkov.[2] This phenomenon, known as the Richtmyer–Meshkov (RM) instability is a typical mechanism for turbulent mixing of layered fluids and is of critical importance to inertial confinement fusion.

RM instability is usually studied in shock tubes, where measurements are easier to carry out than in small pellets.[3–7] In almost all the shock-tube experiments, two gases, a heavy one and a light one, are initially separated using a thin plastic membrane which is often placed directly below a thin wire mesh.[4,6,7] The membrane is then broken into small pieces by the incident shock wave passing through the grid. Shock-tube experiments provide mostly schlieren visualizations for the mixing-zone thickness.[3,4] This diagnostic gives only qualitative information about the intensification of mixing. More quantitative information is obtained by x-rays and differential interferometry measurements,[5] or by infrared absorption.[6] These diagnostics give the density profiles in the mixing zone. The thickening of these density profiles with time is then often attributed to turbulent diffusion in the mixing zone. After the interaction of the reflected shock at the end wall with the mixing zone, a relative intensification of the density fluctuation is sometimes observed and tends to confirm that the flow is turbulent.[6] But all the profiles are averaged along the shock-tube thickness and are consequently deformed by the presence of boundary layers which develop on the shock-tube walls. So, their interpretation remains difficult. Finally, in all previous experiments, the diagnostics give only an indirect measurement of turbulence: Intensification of mixing or intensification of averaged density fluctuations. Furthermore, there is no evidence of turbulence in the mixing before its interaction with the first reflected shock. Therefore, the new experiments performed by Poggi *et al.* are of particular interest.[7,8] In these experiments, instantaneous velocities in a gaseous mixture arising from the shock-wave-induced Richtmyer–Meshkov instability are measured by Laser Doppler Anemometry (LDA). These experiments give for the first time a direct measurement of turbulence. Experimental data demonstrate that the initial small scale perturbations of the interface develop into a turbulent mixing zone after the incident shock-wave passage. Velocity measurements clearly show the strong amplification of turbulence when the shocks reflected at the end wall interact with the mixing zone. Furthermore, data exhibit a decrease of the turbulence level between two successive reshocks, which is explained by both diffusion and dissipation.

Numerous numerical studies have been performed on the RM instability. The first Lagrangian simulations are reported by Meyer and Blewett.[9] Some years after, Cloutman and Wehner performed two- and three-dimensional simulations based on both the Euler and Navier–Stokes equations with a finite difference numerical method and a front-tracking technique.[10] All these computations of the RM instability for singly shocked, sinusoidally perturbed interfaces predict growth rates greater than observed in single-interface experiments. Only recent computations show agreement with ex-

[a)]Electronic mail: claude.mugler@cea.fr

perimental growth rates. First, this agreement has been attributed to the use of a front-tracking technique.[11,12] A front-tracking technique seems well adapted to describe large-scale structures but it cannot be used to simulate turbulent gaseous flows. In this case, a mixing model which describes gaseous mixing at a molecular level is needed. Nowadays, other numerical methods give as good results as a front-tracking technique. For example, 2D (two-dimensional) numerical simulations of the RM instability at two nearby interfaces performed with an Adaptative Mesh Refinement (AMR) Eulerian code show flow patterns in agreement with experimental images.[13] This AMR code and the front-tracking code were compared together with single-mode RM experiments performed with strong radiatively driven shocks.[14] The two numerical techniques agree on the large-scale structures, such as the amplitude of the interface perturbation, and both of them are able to describe experimental data. Other 2D numerical simulations of single-mode RM experiments performed with an Arbitrary Lagrangian–Eulerian (ALE) code also give flow patterns very similar to experimental pictures.[15] In these simulations, mixing of two gases is described within the single fluid approximation by using a concentration governed by an advection-diffusion equation. Numerical and experimental growth rates are in good agreement and are decaying in time in a similar way. All these computations show that experimental and numerical flow patterns are very similar provided the experimental initial conditions (amplitude and wave number of the perturbation) are well known.

The goal of our project is to perform highly resolved three-dimensional numerical simulations of flows subsequent to the RM instability, in order to study both the transitional and the turbulent regimes. Since the Reynolds number of such flows is moderate,[16] direct numerical simulations seem to be feasible. In such an approach, the whole method — physical models, numerical schemes, implementation and resolution — is first confronted with experimental data. Then, numerical results processing gives access to physical quantities, such as vorticity, energy spectrum or statistical correlations, that cannot be measured or extracted from measurements.

In this paper, we apply this general strategy to two-dimensional calculations. As already stated, the whole method is confronted with the experimental data of Poggi *et al.*[7,8] At this stage, experimental data are directly compared with the numerical results in order to interpret the experiments. These shock-tube experiments of SF_6 incident on air demonstrate that the initial small-scale perturbations of the interface develop into a turbulent mixing zone, whose turbulence level decays before the first reflected shock wave arrives from the end wall. Afterwards, the reshock interaction amplifies the turbulence level through a baroclinic effect. Experimental measurements also show that the turbulent boundary layers which develop on the shock-tube walls accelerate the fluid flow in the middle of the tube. Numerical simulations clearly reproduce both this acceleration and the lambda-shock structure observed in experiments. In a second step, we perform a detailed study of the numerical results. In particular, we show that right after the first shock passage the flow still depends on the initial conditions through the large scales although a k^{-3} energy spectrum may be exhibited. After the first reshock, the flow also exhibits a k^{-3} energy spectrum. Moreover, we can see in numerical simulations the scenario detailed above, i.e., decay of the turbulence before the first reflected shock wave–mixing zone interaction and amplification by reshocks.

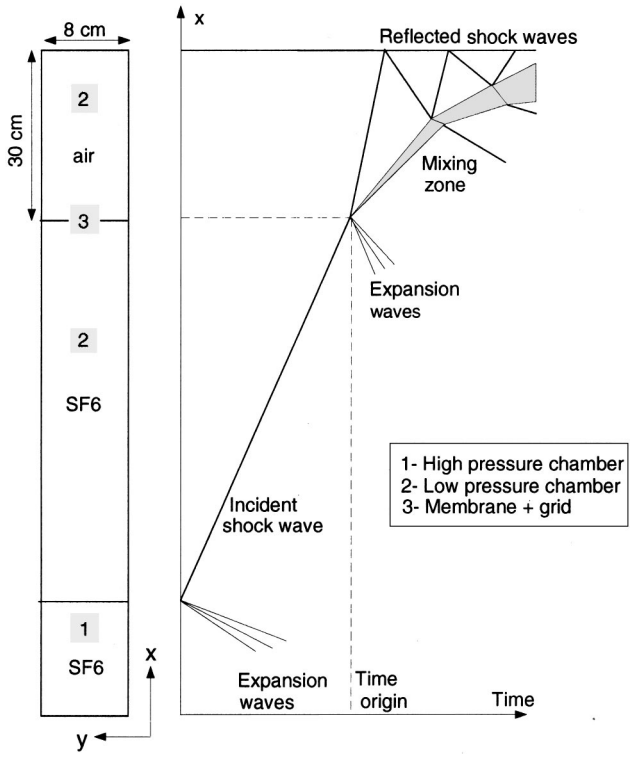

FIG. 1. Schematic shock tube and (x, t) diagram (Ref. 8).

Experimental conditions will be described in Sec. II of this paper. Afterwards, Sec. III will give a description of the numerical methods used to perform the high-resolution simulations. In Sec. IV, experimental measurements and numerical results will be compared, and, finally, in Sec. V, a detailed study of the numerical results will be presented and discussed.

II. EXPERIMENTS

In the experiments performed in the vertical shock-tube at C.E.A.[7,8] a discontinuous heavy-light interface between hexafluoride (SF_6) and air is impulsively accelerated by an incident upward shock wave (Mach number 1.45, shock strength 0.54) and decelerated by several reshocks of decreasing strength (0.38 for the first reflected shock, 0.15 for the second one), as shown in Fig. 1. The shock strength is defined as the pressure jump across the shock front normalized by the pressure behind the shock. The initial Atwood number, defined as $(\rho_2-\rho_1)/(\rho_2+\rho_1)$ where ρ_1 is the density of the first shocked fluid (here the SF_6), is equal to -0.67. The tube has a square cross section ($80\times 80\,mm^2$) with high (5 bar) and low-pressure (1 bar) chambers, 0.8 and 2.96 m long, respectively. The distance between the initial interface position and the upper end wall is set to 0.3 m. The

two gases, the heavy one (SF_6) and the light one (air), are initially separated by a plastic membrane 0.3 μm thick, which is placed directly below a thin wire mesh (wire spacing and diameter: 1.01 and 0.08 mm). The membrane is broken into small pieces by the passing incident shock wave through the grid. Therefore, the initial wavelengths of the perturbations at the SF_6–air interface are supposed to be of the order of the mesh size.

A schlieren visualization allows us to measure the time-dependent location and thickness of the mixing zone. Another diagnostic, the Laser Doppler Anemometry (LDA), gives measurements of the fluctuating flow velocity at selected points in the shock tube. A detailed description of the setup and the characteristics of the diagnostics can be found in Ref. 7.

III. EQUATIONS AND NUMERICAL CHOICES

A. Governing equations

The code CADMÉE, derived from CFDLIB,[17] was developed in order to carry out two-dimensional numerical simulations of unsteady compressible mixing flows, such as those occurring in shock tubes. Features of the modeling are the following:

(i) CADMÉE solves the 2D unsteady full Navier–Stokes equations, namely, the mass, momentum, and energy conservation equations for a viscous, compressible fluid:

$$\frac{\partial \rho}{\partial t}+\frac{\partial}{\partial x_\ell}(\rho u_\ell)=0,$$

$$\frac{\partial}{\partial t}(\rho u_i)+\frac{\partial}{\partial x_\ell}(\rho u_i u_\ell)=-\frac{\partial P}{\partial x_i}+\frac{\partial \sigma_{i\ell}}{\partial x_\ell}, \tag{1}$$

$$\frac{\partial}{\partial t}(\rho E)+\frac{\partial}{\partial x_\ell}(\rho E u_\ell) =-\frac{\partial}{\partial x_\ell}(P u_\ell)+\frac{\partial}{\partial x_\ell}\left(\chi \frac{\partial}{\partial x_\ell}T\right)+\frac{\partial}{\partial x_\ell}(\sigma_{jl}u_j).$$

In these equations ρ is the mass density, T, the temperature, P, the pressure, u_i with $i=1,2$, the material velocity component in the x_i direction, with $x_1 \equiv x$ and $x_2 \equiv y$, $E=e+u_i u_i/2$, the mass specific total energy, e, the mass specific internal energy, and χ, the thermal conductivity coefficient. The components σ_{ij} of the viscous stress tensor $\bar{\bar{\sigma}}$ are defined in the Stokes approximation by

$$\sigma_{ij}=\mu\left(\frac{\partial u_j}{\partial x_i}+\frac{\partial u_i}{\partial x_j}-\frac{2}{3}\delta_{ij}\frac{\partial u_\ell}{\partial x_\ell}\right), \tag{2}$$

where μ is the dynamic viscosity coefficient.

(ii) Mixing of two gases is described within the single fluid approximation by a concentration governed by an advection-diffusion equation which writes

$$\frac{\partial}{\partial t}(\rho c)+\frac{\partial}{\partial x_i}(\rho c u_i)=\frac{\partial}{\partial x_i}\left(\rho D \frac{\partial c}{\partial x_i}\right). \tag{3}$$

where D is the diffusion coefficient. Partial densities of fluids 1 and 2, ρ_1 and ρ_2, are equal to ρc and $\rho(1-c)$, respectively. By doing so, no numerical interface and no mixed cells are needed.

(iii) The pressure P and the density ρ are the sum of the partial pressures and densities of each component, respectively. They are related to temperature by the perfect gas law. The local thermal equilibrium hypothesis is assumed, which implies that the temperature is the same for each species

$$P=P_1+P_2,$$

$$\rho=\rho_1+\rho_2,$$

$$T=T_1=T_2,$$

$$P_i=\rho_i\frac{\mathcal{R}}{\mathcal{M}_i}T=(\gamma_i-1)\rho_i c_{v_i}T, \quad i=1,2.$$

The indices refer to the partial corresponding quantities of fluids 1 and 2. The ratio of specific heats of the mixture, noted γ, can be evaluated with help of the following relations:

$$\gamma=\frac{c_{p_{\text{mixing}}}}{c_{v_{\text{mixing}}}}=\frac{c c_{p_1}+(1-c)c_{p_2}}{c c_{v_1}+(1-c)c_{v_2}} =\frac{c c_{v_1}\gamma_1+(1-c)c_{v_2}\gamma_2}{c c_{v_1}+(1-c)c_{v_2}}. \tag{4}$$

The specific internal energy of the mixture is written

$$e=c_{v_{\text{mixing}}}T=(c c_{v_1}+(1-c)c_{v_2})T. \tag{5}$$

With these hypotheses, the sound speed c and the Mach number M are defined as

$$c^2=\frac{\gamma P}{\rho}, \quad M=\frac{||\mathbf{u}||}{c}. \tag{6}$$

(iv) Viscosity and molecular diffusion coefficients of each species of the mixture are calculated from Ref. 18. Thermal conductivity coefficients can be obtained directly from viscosity coefficients provided the Prandtl number of each species is assumed to be constant. Mixture viscosity and molecular diffusion coefficients are then determined from Wilke's mixture rule[19] and the mixture thermal conductivity coefficient is calculated from the model given in Ref. 20. Finally, all transport coefficients, (viscosity, diffusion, and thermal conductivity), depend on the two thermodynamic quantities: concentration and temperature.

B. Description of the numerical choices

Features of the numerical method are detailed in Ref. 21 but let us recall here the main characteristics of the code CADMÉE:

(i) CADMÉE uses structured meshes made of quadrangular cells;
(ii) state variables are cell-centered;
(iii) a Godunov method is used to accurately describe strong discontinuities such as shock waves. It uses the

approximate Riemann solver of Dukowicz.[22] Consequently, no artificial viscosity is needed;

(iv) a second-order differencing technique in space can be used and a low-storage second order Runge–Kutta scheme has been implemented.[23] The importance of the scheme accuracy has been shown in a previous paper;[15]

(v) the computation is performed in two phases: A Lagrangian phase and a remapping phase in which conservative variables are transferred from the Lagrangian mesh to an arbitrary specified mesh. This approach is the so-called Arbitrary Lagrangian–Eulerian (ALE) formulation;

(vi) Although the code solves the 2D Navier–Stokes equations, a turbulent algebraic model, the Baldwin–Lomax model,[24] has been implemented in order to model turbulent boundary layers that usually develop along shock tube walls. Indeed, direct numerical simulations of transition and turbulence in the boundary layers would have required higher spatial resolutions. Furthermore, it would have been necessary to define the characteristics of the perturbations which destabilize the boundary layers. In experiments, schlieren pictures clearly show that the boundary layers are turbulent. Several defects on the shock-tube walls certainly contribute to the transition, but they are not well identified. So, as we are not interested in the boundary layers themselves but only in their effects on the flow, we prefer using a well-known turbulent model which acts only near the walls. The Baldwin–Lomax model is a two-layer eddy viscosity model in which the turbulence effects are modeled through the expression of turbulent transport coefficients which are added to the molecular transport coefficients in the Navier–Stokes equations. The turbulent eddy viscosity μ_t is given by

$$\mu_t = \begin{cases} (\mu_t)_{\text{in}} & 0 \leqslant y \leqslant y_c \\ (\mu_t)_{\text{out}} & y_c \leqslant y \leqslant \delta, \end{cases}$$

where y is the normal distance from the wall and y_c can be defined as the smallest value for which the two formulations are equal. Consequently, the turbulent model does not act far from the walls.

The code CADMÉE has been validated against numerous configurations of compressible viscous flows.[21] Of particular importance to the computations reported in this paper is the fact that we are performing direct 2D numerical simulations. Indeed, as already stated, the Baldwin–Lomax turbulence modeling used here acts only near the walls.

IV. COMPARISON OF EXPERIMENTS AND SIMULATIONS

A. Initial configurations

The definition of the initial hydrodynamic conditions for the computations is based on shock-tube experiments previously described. As said before, the CEA shock tube is vertical. However, out of habit, the simulated shock tube will be horizontal. This rotation does not have any consequence in the configuration studied because gravity effects can be neglected. In numerical simulations, the initial perturbation of the interface is multimode and composed of eight wavelengths λ of the order of the experimental wire mesh size: $\lambda = 0.5$, 0.625, 0.8, 1, 1.25, 1.6, 2, and 2.5 mm. As we shall see below, before the reshock, the evolution of the mixing-zone width depends on the characteristics of the initial perturbations at the interface. So, in computations, we assume that the wavelengths are of the order of the experimental wire mesh size but we have no experimental information on the amplitude values. So, we arbitrarily take the same value for all the amplitudes. This value, equal to 0.2 mm, has been deduced from several simulations — performed with a coarser numerical grid than those used below in this section — in order to obtain, before the reshock, a time evolution of the mixing-zone width in agreement with experimental results. The largest dimensionless initial perturbation amplitude ak is equal to 0.25. The initial shock Mach number is equal to 1.453. Calculations are started with a Lagrangian mesh with nodes located at the initial interface, and continued with an Eulerian grid before the shock reaches the interface. By doing so, the development of undesired perturbations of wavelengths of the order of the numerical mesh size is avoided. The instant $t = 0$ corresponds to the moment the shock strikes the left edge of the perturbation.

The purpose of numerical and experimental studies is twofold: First, to study the evolution of the turbulent mixing zone and second, to quantify the influence of the turbulent boundary layers on the fluid dynamics in the middle of the tube. Only one simulation to accurately simulate both the mixing zone and the boundary layers would have required too many zones in the mesh. Therefore, two kinds of simulations of the experiment have been performed. They principally differ by the mesh and the boundary conditions used.

In the first kind of simulations, only a half-shock-tube is simulated and the walls are considered as reflective walls. The mesh zone size is regular in the transverse direction y but not in the longitudinal direction x. Two runs have been carried out with two various zone sizes in the y direction. The region where the instability initially develops is covered with $0.05 \times 0.08\,\text{mm}^2$ zones in the coarse grid and $0.05 \times 0.05\,\text{mm}^2$ zones in the fine one. At last time, the mixing zone moves in a region covered with $0.7 \times 0.08\,\text{mm}^2$ and $0.7 \times 0.05\,\text{mm}^2$ zones in the coarse and fine grids, respectively. The entire coarse (fine) mesh is done of 500 000 (720 000) zones.

In the second kind of simulation, the entire shock tube is simulated and no slip type boundary condition for the velocity and isotherm type ($T_w = 293$ K) boundary conditions for the temperature are assumed. Furthermore, turbulent boundary layers are computed with the Baldwin–Lomax model. The mesh is refined near the walls in order to accurately simulate the boundary layers: The lowest transversal zone size is equal to 0.05 mm and the largest one is equal to 0.78 mm. The entire mesh is done of 500 000 zones.

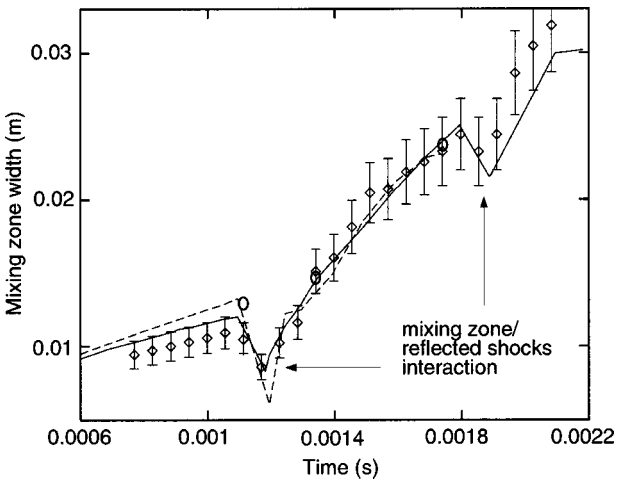

FIG. 2. Evolution of the mixing-zone width vs time. Diamonds correspond to the experimental width measured from schlieren pictures. The errorbars of this visual measurement are equal to $\pm 10\%$. The three small circles correspond to microdensitometry measurements of some schlieren pictures. Full and dotted lines correspond to numerical widths obtained from the coarse and fine grids, respectively.

B. Mixing-zone width

In the experiments, a schlieren visualization allows us to measure the mixing-zone thickness. To estimate the mixing-zone width from the numerical simulations, we calculate in each abscissa x the transversal averaged density $\rho_m(x)$. The density profile is then normalized and the mixing-zone width is defined as the distance between the two points where the normalized density is equal to 0.97 and 0.03. Figure 2 displays the evolution versus time of the experimental and numerical mixing-zone widths. Diamonds correspond to the experimental width measured from schlieren pictures. The errorbars of this visual measurement are equal to $\pm 10\%$. The three small circles correspond to microdensitometry measurements of some schlieren pictures. In Fig. 2, compressions due to the interaction of the reflected shock waves with the mixing zone clearly appear. Before the first reflected shock–mixing zone interaction, microdensitometry gives mixing-zone width greater than those obtained from direct measurement from optical pictures. The discrepancy between experimental results before the first reflected shock–mixing zone interaction may be attributed to the difficulty to correctly distinguish the initially thin mixing zone from the turbulent boundary layers which develop on the shock-tube walls. In Fig. 2, full and dotted lines correspond to mixing-zone width values calculated from numerical simulations with the coarse and fine grids, respectively. After incident shock–interface interaction and before the interaction of the mixing zone with the first reflected shock at the end wall tube, the mixing-zone width calculated from the simulation obtained from the finest mesh is larger than the other one. This discrepancy may be due to the small wavelengths which are smoothed when the mesh is not fine enough. Previous numerical simulations of single-mode Richtmyer–Meshkov experiments have shown that 50 mesh zones in the wavelength are necessary to correctly describe the evolution of the amplitude perturbation and a very high spatial resolution (360 mesh zones in the wavelength) is required if we want the physical viscous dissipation to dominate the numerical viscosity effects.[15] The finest resolution used in the present simulations corresponds to only 10 and 50 zones in the smallest and largest wavelengths, respectively. Consequently, only the largest wavelengths which are very close to the experimental mesh size are sufficiently described. On the other hand, the calculation of the small wavelengths is not converged and is responsible for the difference between the results obtained from the coarse grid and the fine grid numerical simulations. However, after the first reflected shock–mixing zone interaction, Fig. 2 shows that the mixing-zone widths obtained from the coarse and the fine meshes are very similar. It looks as if the grid resolution had no more effect on the mixing-zone width. This spatial convergence is achieved because larger and larger structures develop in the mixing zone and both numerical grids are fine enough to describe them. Spectral analysis presented in next section will confirm this result. Figure 2 allows us to compare numerical results with experimental ones. After the incident shock passage and before the reshock, mixing-zone widths obtained from numerical simulations are slightly greater than experimental ones. This result is not surprising since the values of the amplitudes of the initial perturbations have been chosen with this aim from numerical simulations performed with a coarser grid. After the first interaction and before the second one, experimental and numerical widths are very similar. In experiments, according to Vetter and Sturtevant,[4] the thin membrane which forms the initially plane interface has a significant influence on the initial growth rate of the mixing-zone thickness. On the other hand, the measured growth rates after the first reflected shock–mixing zone interaction are independent of the membrane configuration.

C. Velocity in the mixing zone

As we said previously, the experiments performed at the C.E.A. use the Laser Doppler Anemometry (LDA). This diagnostic gives measurements of the fluctuating flow velocity which can be directly compared with results of numerical simulations. In the experiments[7,8], the position of the LDA probe is successively at 125.5, 161, and 178.5 mm downstream the initial interface abscissa. Figure 3 shows velocity measurements at the abscissa 161 mm. In this figure, diamonds correspond to experimental data.[8] The full line corresponds to the numerical simulation obtained with the fine resolution in the mixing zone, without turbulent boundary layers. Hereafter, the instant $t=0$ corresponds to the moment the shock arrives at the probe. In Fig. 3, the first experimental velocity plateau at 130 m/s corresponds to air accelerated by the incident shock wave (for $t \leqslant 0.8$ ms). Then we observe a second perturbed plateau which includes the crossing of the turbulent mixture. The Rankine–Hugoniot relations give a theoretical mean velocity of 47 m/s in this plateau although experimental measurements give a mean velocity of 59 m/s. This acceleration is due to the boundary layer reversal effects in the SF_6 at shock crossing decelerated by the first reflected shock on the end wall. This second plateau ends with the arrival of the second reflected shock wave. In Fig. 3 the

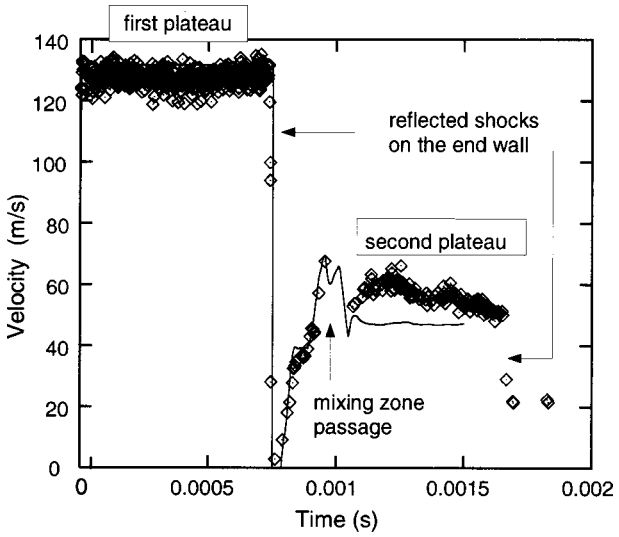

FIG. 3. Velocity measurements at 161 mm. Diamonds correspond to experimental data. The full line corresponds to the numerical simulation obtained with the fine resolution in the mixing zone, without turbulent boundary layers.

numerical velocity fluctuates in the mixing zone and the levels of the fluctuations are the same as the experimental ones. These low-frequency fluctuations can be correlated to spatial structures which develop in the mixing zone. In Figs. 4(a) and 4(b), three isovalues of the concentration of SF_6 in the mixing zone ($c=5\%$, 50%, and 95% from right to left) are superimposed on the velocity colormaps at two various instants, just before [Fig. 4(a)] and just after [Fig. 4(b)] the first reflected shock–mixing zone interaction. In Fig. 4(a), the zones where the velocity is higher than the averaged value 131.5 m/s correspond to heavy gas pockets which penetrate in the light gas. On the other hand, the zones where the velocity is lower than the value 131.5 m/s correspond to light gas pockets which are pushed by the heavy gas. After the reflected shock passage through the mixing zone [Fig. 4(b)], the difference in velocity between air bubbles and SF_6 spikes is bigger.

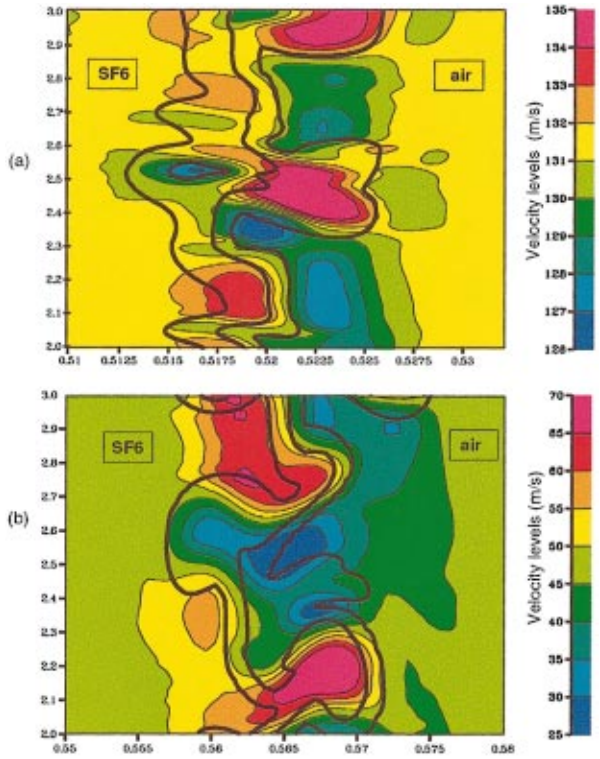

FIG. 4. (Color) Superimposition of concentration isocontours and velocity colormaps: (a) Before and (b) after the first reflected shock passage.

D. Effects of the boundary layers

Experimental measurements show that the turbulent boundary layers which develop on the shock-tube walls perturb the fluid dynamics in the middle of the tube. High-resolution 2D numerical computations with no slip type boundary condition for the velocity and isotherm type boundary condition for the temperature allow us to simulate this behavior. Figure 5(a) gives an example of density numerical isocontours in the mixing zone. It shows that the mixing zone is stretched along the shock tube walls in the boundary layers. Therefore, the density profiles obtained by

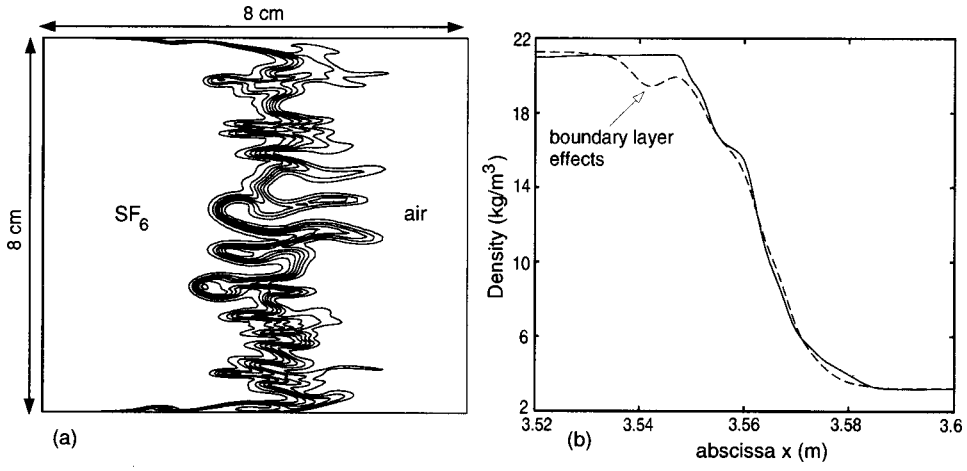

FIG. 5. Stretching of the mixing zone by the turbulent boundary layers which develop on the shock-tube walls: (a) Density isocontours and (b) density profiles obtained by taking the average of the density on all the shock-tube thickness (dotted line) or only in the middle of the tube (full line).

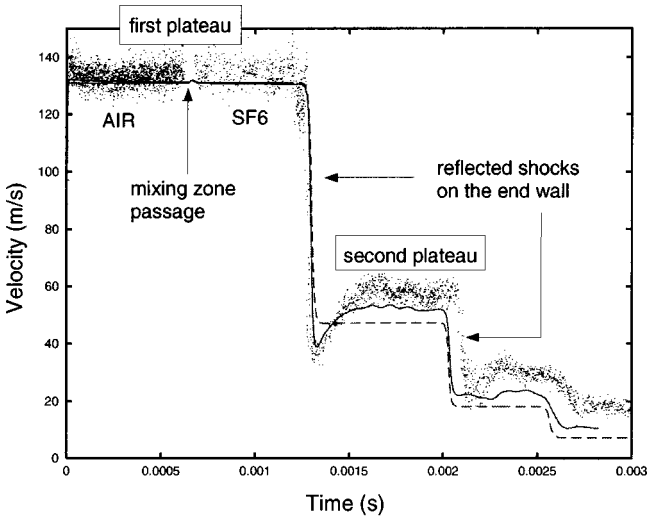

FIG. 6. Velocity measurements at 125 mm. Dots correspond to experimental data. Full and dashed lines correspond to numerical simulations with and without turbulent boundary layers, respectively.

taking the average of the density on all the shock tube thickness [dotted line in Fig. 5(b)] or only in the middle of the tube [full line in Fig. 5(b)] are not the same. As the experimental microdensitometry measurements of the mixing-zone width consist in calculating averaged density profiles from schlieren pictures which include boundary layer effects, it is not surprising to find a higher value than the width visually measured (see crosses and diamonds in Fig. 2). LDA measurements with the probe located at 125.5 mm downstream the initial interface abscissa allow us to study boundary layer effects. Figure 6 shows velocity measurements at this abscissa. In this figure, dots correspond to experimental data. Full and dashed lines correspond to numerical simulations with and without turbulent boundary layers, respectively. The instant $t=0$ corresponds to the moment the shock arrives at the probe. In Fig. 6, the first velocity plateau at 130 m/s firstly corresponds to air accelerated by the incident shock (for $t \leqslant 0.6$ ms) and afterwards to SF_6. The second plateau at 59 m/s corresponds to SF_6 decelerated by the first reflected shock on the end wall. This second plateau ends with the arrival of the second reflected shock wave. As one can see in Fig. 6, one effect of the turbulent boundary layers is to accelerate the SF_6. The first simulation, whose results in pure gases are similar to the Rankine–Hugoniot solutions, gives a theoretical mean velocity of 47 m/s in the second plateau, while experimental measurements give a value of 59 m/s. In the 2D simulations presented in this paper, only two turbulent boundary layers are simulated and the mean velocity in the second plateau equals 52 m/s. By simulating with a 3D (three-dimensional) code the four turbulent boundary layers which really develop in the shock tube, we may expect to find a higher value close to the experimental one.

Another effect of the turbulent boundary layers is the velocity undershoot just after the passage of the first reflected shock. As this shock interacts with the mixing zone, a shock (Mach number equal to 1.37 in fluid-fixed reference frame) is transmitted in the SF_6. Because of its interaction with the boundary layer in the SF_6 and according to the hydrodynamic conditions (Mach number and adiabatic coefficient values), this transmitted shock bifurcates. The experimental interferometric image given in Fig. 7(a) clearly shows the lambda shock structure, with the presence of a bubble at the shock foot.[5] The bifurcation height increases as the shock moves in the SF_6. Figure 7(b) shows the numerical schlieren-type image obtained at the same instant. Such numerical images are particularly useful to simultaneously visualize mixing-zone and shock structures. As shown in Fig. 7, the visual agreement between the experimental schlieren picture and the numerical schlieren-type image is very good for the shock structure. On the other hand, the numerical mixing zone is thicker than the experimental one. This dis-

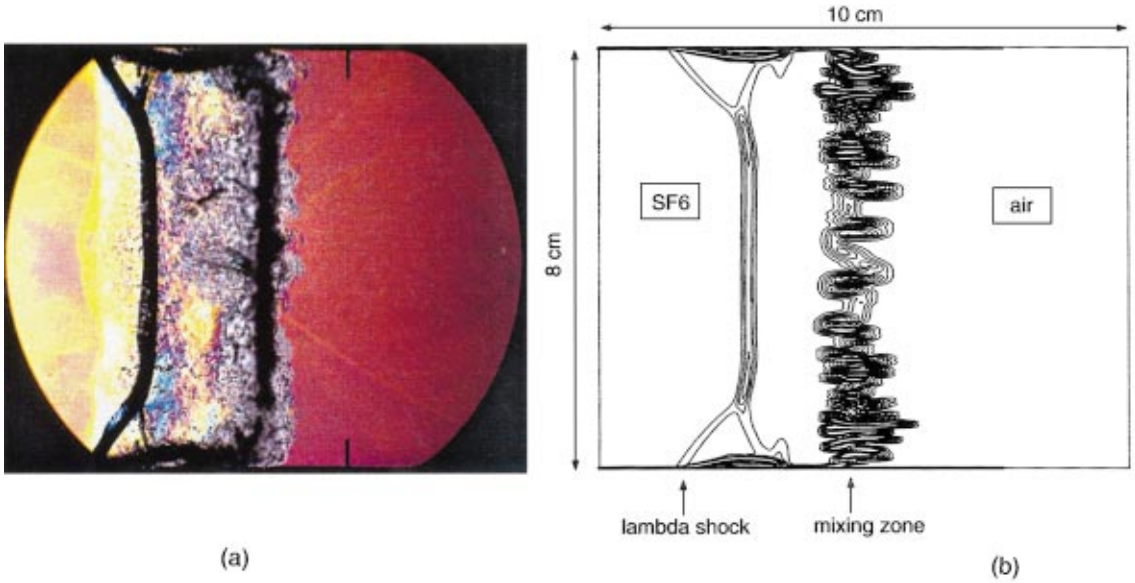

FIG. 7. (Color) (a) Experimental, from Galametz (Ref. 5), and (b) numerical schlieren pictures at a time t just after the first reflected shock wave–mixing zone interaction. Because of its interaction with the boundary layer, the transmitted shock in the SF_6 bifurcates.

crepancy has two reasons. First, the numerical image has been obtained from the computation performed with a high-spatial resolution near the walls. Consequently, the turbulent boundary layers and their interaction with the refracted shock wave are well described, but not the mixing zone which is too diffuse. Second, this nice experimental interferometric image has been obtained from previous experiments.[5] In these experiments, the plastic membrane which initially separates the heavy gas from the light one is not placed directly below a thin wire mesh. Consequently, the membrane is not broken into small pieces by the incident shock and it slows down the mixing of the two gases. The experimental mixing-zone thickness is then thinner than expected. The influence of the boundary layers on the flow at the middle of the tube points out the interest of building shock tubes with larger cross-sectional areas, as it has been done by Vetter and Sturtevant.[4]

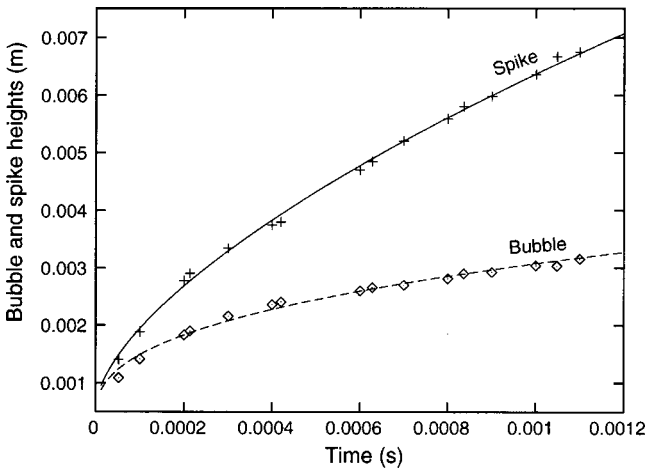

FIG. 8. Evolution of large stuctures in the RM mixing fronts. Crosses and diamonds correspond to spike and bubble heights, respectively. Full and dotted lines correspond to power laws $L(t)=L_1 t^{\beta}$ with $\beta_s=0.63$ for the spike front and $\beta_b=0.39$ for the bubble front.

V. ANALYSIS OF THE NUMERICAL RESULTS

A. Scaling laws

In a general way, it is of interest to look for scaling laws for the evolution of the mixing-zone width. In that respect, several interpretations of the numerical results can be given. First, models for the nonlinear regime such as those proposed by Ramshaw[25] and Alon *et al.*[26] may be used. Second, statistical models of fully developed turbulence may also be used.[27,28] For example, the solution of the diffusion-dissipation part of a two-equation k-ϵ model provides a self-similar behavior that can be compared with numerical results.

The first approach to model the evolution of the mixing zone gives a lot of importance to the nonlinear behavior of large structures in the mixing fronts. A numerical study has been performed by Alon *et al.*[26] in order to validate a 2D model based on bubble-rise dynamics. This theoretical and numerical study of the nonlinear evolution of large structures in RM mixing fronts gives a constant power-law coefficient β_b equal to 0.4 for multimode RM bubble fronts. On the other hand, the power-law coefficient β_s for the spike fronts is not constant: It increases with the Atwood number A_t from $\beta_s=0.4$ for $A_t=0$ to $\beta_s=1$ for $A_t=1$. According to Fig. 2 from Ref. 26, β_s is approximately equal to $(1+A_t)\beta_b$. In our case, the Atwood number is equal to -0.67 whence the β_s value is equal to 0.66. Figure 8 displays the evolution versus time of the large stuctures in the RM mixing fronts. In numerical simulations, spike and bubble heights are inferred from the location of bubble and spike fronts relative to the unperturbed interface. The location of the unperturbed interface is obtained from the calculation of the theoretical interface velocity with the Rankine–Hugoniot relations. In Fig. 8, crosses and diamonds correspond to spike and bubble heights, respectively. Full and dotted lines correspond to the fits of the numerical results by power laws $L(t)=L_1 t^{\beta}$, with $\beta_s=0.63$ for the spike front and $\beta_b=0.39$ for the bubble front. The power-law coefficients β_b and β_s presently obtained from 2D CADMÉE simulations are in good agreement with bubble-rise models ($\beta_b=0.4$ and $\beta_s=0.66$).

In the second approach, by considering self-similar solutions of a one equation statistical turbulent model reduced to the diffusion and dissipation terms, Barenblatt[27] has shown that, at late time, the turbulent width varies as t^{β} with $\beta=2/3$ in the case of zero dissipation and $\beta<2/3$ otherwise. Cherfils and Harrison[28] also studied the evolution of a one-dimensional turbulence in the case where it is completely determined by diffusive and dissipative processes. On the bases of two-equation k-ϵ models, they found a self-similar solution asymptotic to the exact flow. The decay exponent of the kinetic energy was equal to -1.32, -1.39 or -1.48 according to three various numerical values of the dissipation coefficient. This phenomenological dissipation coefficient is usually calibrated on 3D experiments. The layer thickness then scales as t^{β} where $\beta=0.34$, 0.305, and 0.26, respectively. Such power-law behavior has also been found from numerical simulations carried out by several authors. For multiple-scale random perturbations, the layer thickness obtained by Pham and Meiron[29] from 2D RM instability simulations in continuously stratified fluids seems to scale with t^{β}. The time exponent β shows a weak dependency on the initial configurations but it always lies in the neighborhood of 0.25. According to Pham and Meiron, ''the time variation of the layer thickness differs from the scaling derived using ideas of self-similarity due to Barenblatt[27] even at low Atwood ratio, presumably because of the inhomogeneity and anisotropy due to the excitation of vortical plumes.'' Furthermore, ''it is possible that the layer has not evolved over a sufficiently long time. At the end of the calculations the layer has only grown a factor of roughly two over its initial size.'' Youngs[30] obtains a close value $\beta=0.3$ from 3D numerical simulations but he notices ''Richtmyer–Meshkov mixing due to a single shock does depend on the initial conditions, and different forms for the initial perturbations are likely to give different values for the power-law coefficient.'' Very recently, a simple model for linear and nonlinear mixing at unstable fluid interfaces has been proposed by Ramshaw.[25] It reproduces the RM growth

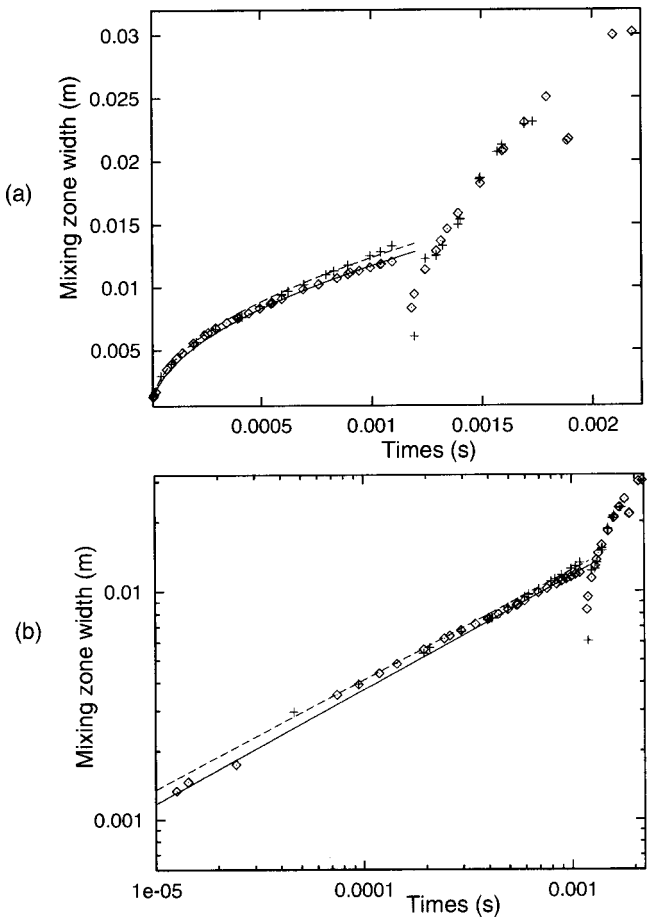

FIG. 9. Mixing-zone width vs time, (a) with a linear scale and (b) with a log–log scale. Diamonds and crosses correspond to numerical simulations with code CADMÉE obtained from the coarse and fine grids, respectively. Full and dotted lines correspond to a power law $L(t)=L_1 t^{\beta}$. The fits of the numerical results give $L_1=0.37$, ($L_1=0.34$), and $\beta=0.50$, ($\beta=0.48$), for the simulation obtained from the coarse (fine) grid.

law $L(t)\sim t^{\beta}$ where β depends on the rate of kinetic energy dissipation: In the case of zero dissipation, it gives the previous theoretical value $\beta=2/3$ first proposed in Ref. 27 and it further exhibits the expected reduction in β due to dissipation.

Figures 9(a) and 9(b) display the evolution versus time of the mixing-zone width with a linear and a log–log scale, respectively. In these figures, diamonds and crosses correspond to numerical simulations obtained from the coarse and fine grids, as previously presented in Fig. 2. In Figs. 9(a) and 9(b), full and dotted lines correspond to a power law $L(t)=L_0+L_1(t-t_0)^{\beta}$. In this expression, $t_0=0$ and $L_0=L(t_0)=0$ because the instant $t=0$ corresponds to the moment the incident shock strikes the discontinuous interface (see Fig. 1). After the incident shock passage and before the reshock, the fit of the numerical results gives $L_1=0.37$, ($L_1=0.34$), and $\beta=0.50$, ($\beta=0.48$), for the simulation obtained from the coarse (fine) grid. The power-law coefficients β presently obtained ($\beta=0.48$ and 0.50) correspond to the complex flow behavior subsequent to the RM instability generated by a single shock wave. So, the power-law coefficients obtained from our simulations ($\beta\approx 0.5$) are in agreement with non zero dissipation ($\beta<2/3$) and are equal to the power-law

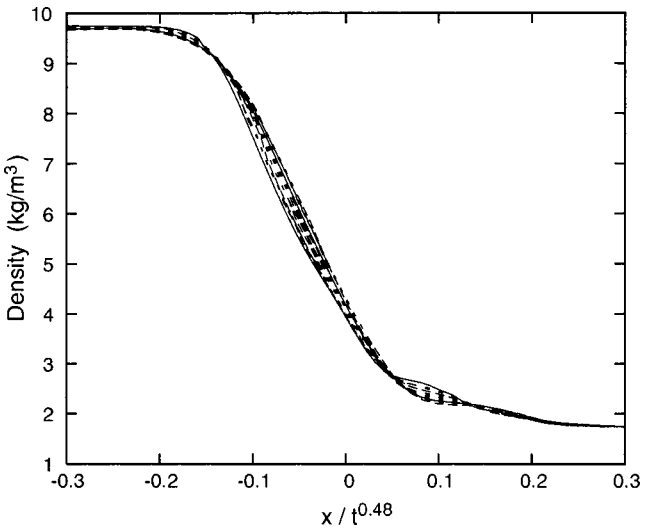

FIG. 10. Transversal averaged density profiles obtained from the fine grid at several times before the reshock and versus the abscissa $\xi=x/t^{0.48}$. These profiles show the quasi self-similar behavior of the mixing-zone.

values reported by Dimonte *et al.* ($\beta=0.5\pm 0.1$) from turbulent Richtmyer–Meshkov instability experiments performed with strong radiatively driven shocks.[31] All these results concern the mixing-zone behavior after the incident shock passage and before the reshock. After the reshock, Fig. 9(b) shows that a power-law is no more valid. Figure 10 gives the transversal averaged density profiles ρ_m obtained from the fine grid simulations at several times and versus the abscissa $\xi=x/t^{\beta}$ with $\beta=0.48$. These profiles show the quasi self-similar behavior of the mixing zone.

B. Spectral analysis

To characterize the flow regime, we study the nonlinear evolution of the interface perturbation by modal analysis, as done in Ref. 15. We introduce the new variable $\mathcal{U}\equiv\sqrt{\rho}u$ where ρ is the density and u the streamwise velocity component. This quantity is equal to the square root of the kinetic energy per unit volume. Then, we consider the one-dimensional transversal spectrum

$$E(k_y,t)=\frac{1}{2L_x}\int_{-L_x}^{+L_x}|\hat{\mathcal{U}}(x,k_y,t)|^2dx. \tag{7}$$

In this expression, $\hat{\mathcal{U}}(x,k_y,t)$ is the transversal discrete Fourier transform of the variable $\mathcal{U}$ at a given abscissa x, it reads

$$\hat{\mathcal{U}}(x,k_y,t)\equiv\hat{\mathcal{U}}\left(x,\frac{\ell}{N\Delta y},t\right)=\frac{1}{N}\sum_{j=0}^{N-1}\mathcal{U}(x,j\Delta y,t)\exp\left(-i\frac{2\pi\ell j}{N}\right), \tag{8}$$

where $\ell=0,1,\ldots,N-1$, N is the number of samples and Δy the sample interval. The length $2L_x\leqslant d$ corresponds to a x-span on which the transversal spectrum is averaged. We will commonly choose d equal to the shock-tube square section and the length $2L_x$ greater than or equal to the mixing-zone width at the final time. The advantage of this spectral

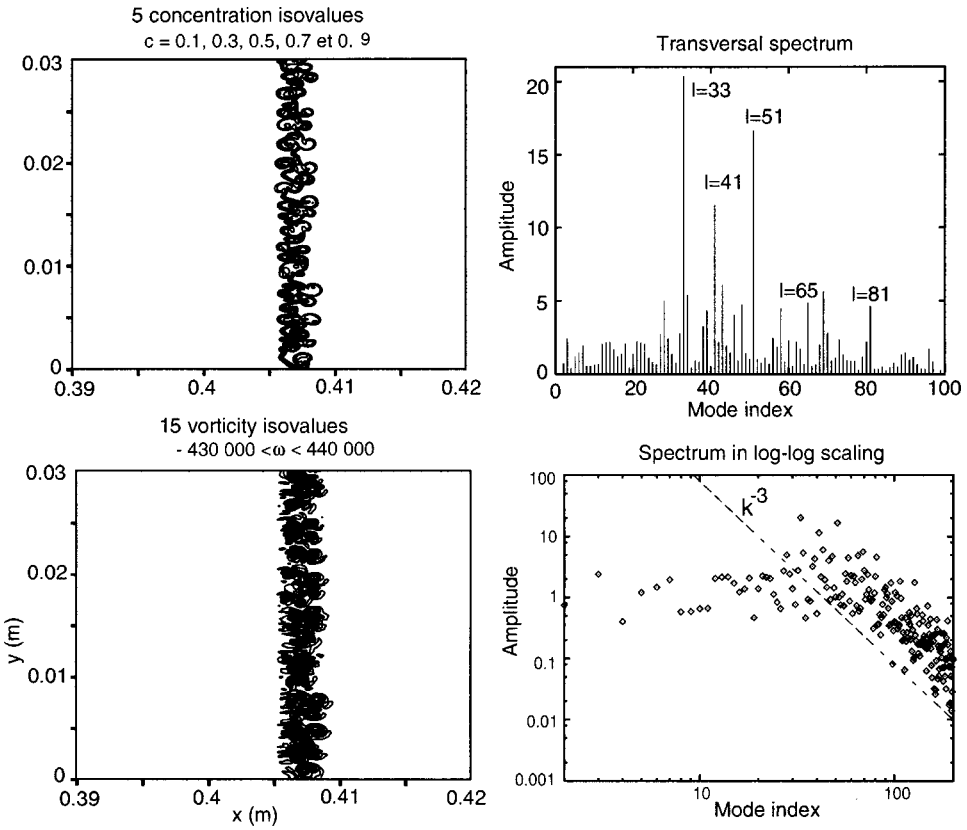

FIG. 11. Concentration isocontours, vorticity isocontours and energy spectrum $E(k_y,t)$ in a linear and in a log–log scale at the instant $t=0.152$ ms, just after the incident shock passage through the initial perturbated interface.

analysis is to give information on all scales present in the mixing zone, even if the flow develops into a turbulent regime. In Eq. (7), the quantity $E(k_y,t)$ represents the spatial average of the streamwise kinetic energy spectral density. The total streamwise kinetic-energy is then given by $\langle E(t)\rangle = \Sigma_{k_y} E(k_y,t)$.

Figures 11–14 give the concentration and vorticity isocontours at four various times. The sizes of the windows are 3 cm width and 3 cm height for all these maps. Figures 11–14 also give the one-dimensional averaged transversal spectra of the quantity $\mathcal{U}$, given by Eqs. (7) and (8), in linear and log–log scales. We have superimposed the k^{-3} enstrophy cascade to the energy spectra. Just after the incident shock–interface interaction (see Fig. 11), the concentration isovalues already show the existence of bubble and spike structures in the mixing zone. The vorticity is concentrated in these structures. The interface perturbations have already evolved into the nonlinear regime. However, the lowest initial perturbation modes are still present and dominant in the energy spectrum. Afterwards, the mixing zone becomes larger and larger and the initial perturbation modes disappear (see Fig. 12). The energy spectrum moves towards the large wavelengths and exhibits the persistence of dominant modes smaller than the initial ones. After the reflected shock passage (Fig. 13), the mixing zone is compressed — as already seen in Fig. 2 — and the vorticity strongly increases through the baroclinic production term. Perturbation modes present in the mixing zone are all excited. However, the spectrum still contains some dominant low modes and shifts towards low wave numbers (see Fig. 14). Spectral analysis quantitatively confirms what can be seen in concentration and vorticity isovalues: Larger and larger spatial structures develop in the mixing zone. Spectra globally move towards low wave numbers and exhibit a k^{-3} enstrophy cascade. This scaling law is valid for a limited range of wave numbers. Indeed, the high wave number end of the spectra is unsignificant because of the mesh-size limitation. For example, the mode index $\ell=101$ corresponds to the wavelength $\lambda=0.8$ mm which is described with only 16 mesh zones. The k^{-3} enstrophy cascade was first predicted by Kraichnan.[32] Kraichnan conjectured that, if energy is fed in at a constant rate to a band of wave numbers of the order of k_i, on one hand, an inverse cascade of energy with constant energy flux will take place following a $k^{-5/3}$ law for $k \ll k_i$ and, on the other hand, a k^{-3} range with constant enstrophy flux will be observed at largest wave numbers for $k \gg k_i$, up to the viscous cutoff. Batchelor[33] also obtained the k^{-3} inertial energy spectrum by phenomenological and dimensional considerations in the context of a freely decaying two-dimensional turbulence, where a self-similar evolving spectrum was assumed. But the confirmation by numerical simulations of this k^{-3} energy spectrum is not so evident.[34] However, the analysis of the relaxation of two-dimensional turbulence performed by McWilliams[35] shows the expected k^{-3} law but also exhibits the emergence of larger scales of turbulence and show that the long-time evolution of two-dimensional fields is dominated by coherent vortices whose vorticities are much stronger than that of the well-mixed background. Finally, the spectral analysis of our numerical simulations tends to prove that the flow in the mixing zone is turbulent. As we will see in the next paragraph, this turbulent behavior is confirmed by statistical analysis.

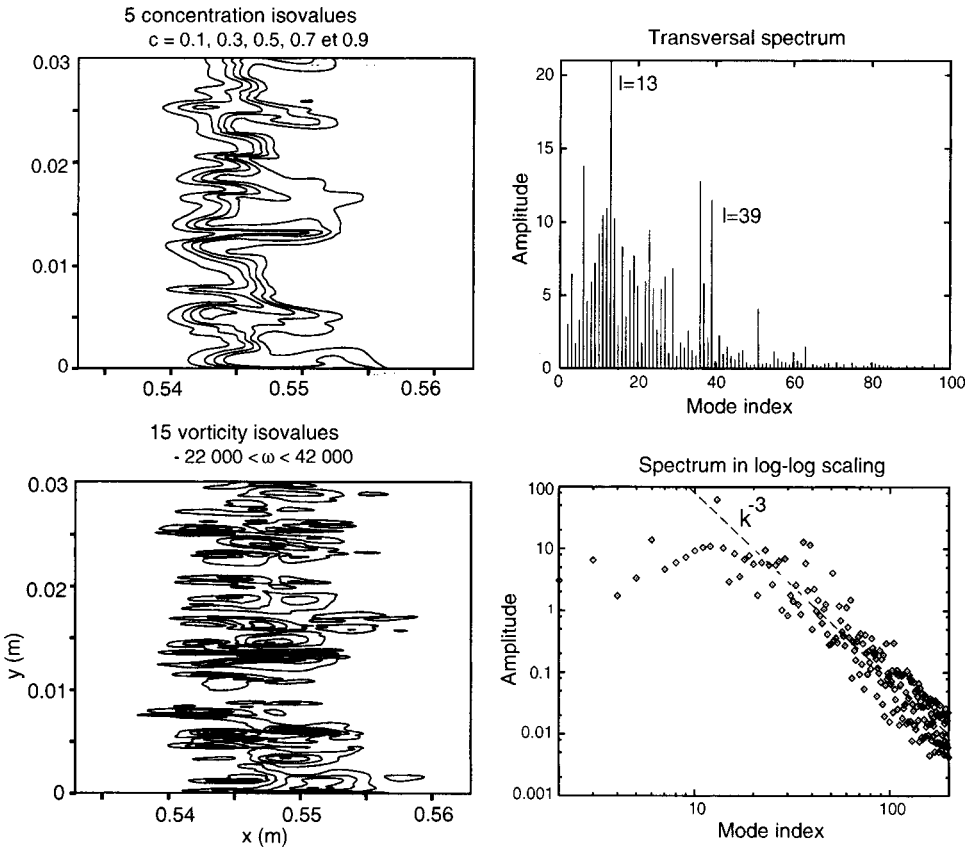

FIG. 12. Same as in Fig. 11 but at the instant $t=1.2$ ms, just before the first reflected shock–mixing zone interaction.

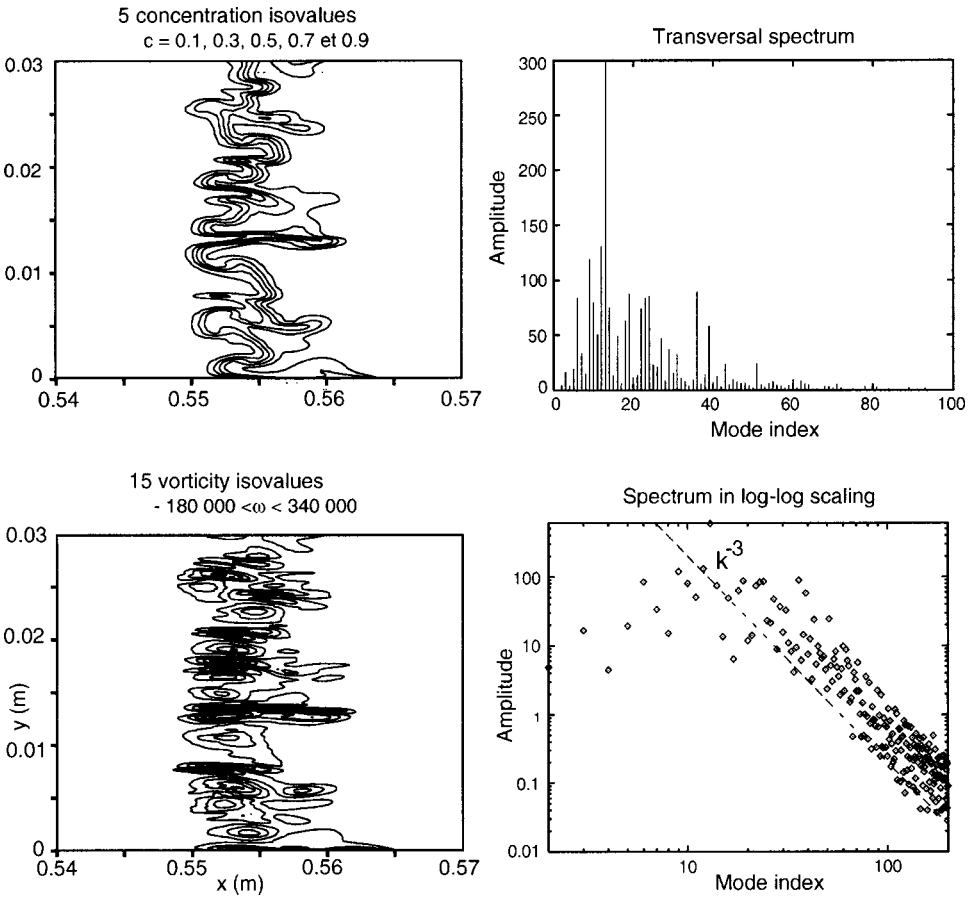

FIG. 13. Same as in Fig. 11 but at the instant $t=1.3$ ms, just after the first reflected shock–mixing zone interaction. The scales of the transversal spectrum have been modified.

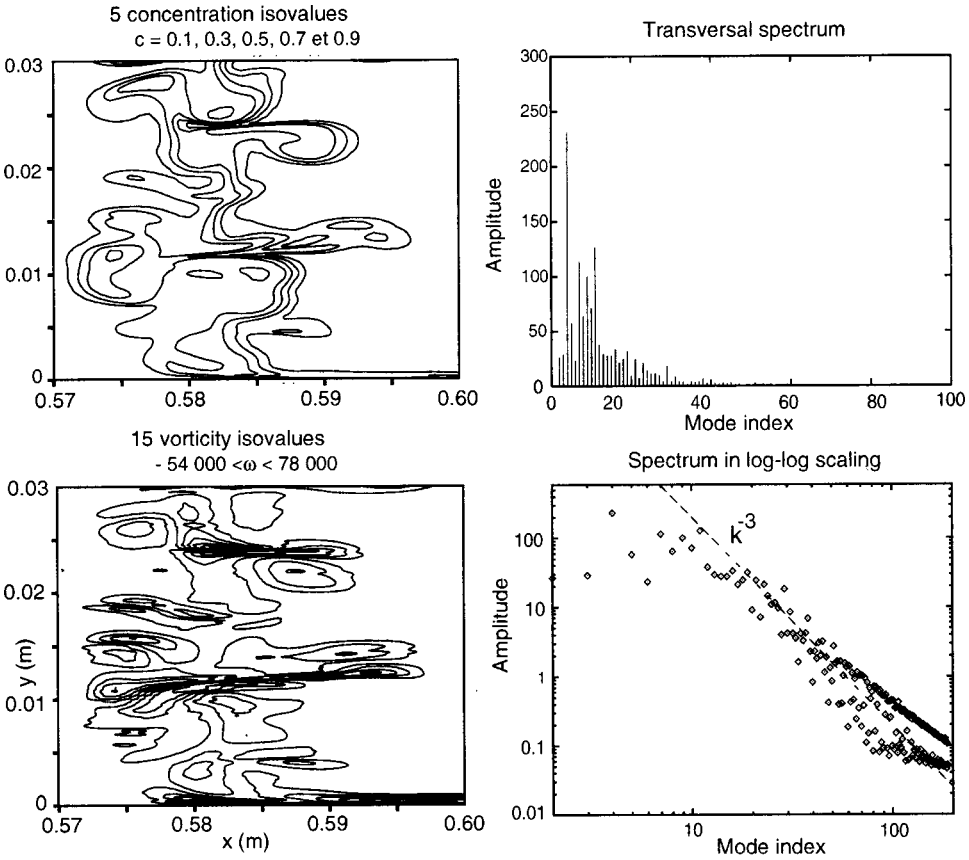

FIG. 14. Same as in Fig. 13 but at the instant $t=1.84$ ms, a long time after the first reflected shock–mixing zone interaction.

C. Statistical analysis

A rigorous study of the statistical properties of compressible Richtmyer–Meshkov instability-induced turbulent mixing would need an average several numerical simulations. In practice, it is not possible yet because we are limited by the excessive memory requirements and long run times. So, hereafter, we use only the fine resolution simulation previously described. In this simulation, there are no boundary layers. Experimental LDA measurements have shown a strong anisotropy of the turbulence in the mixing zone:[7] The most energetic component of the Reynolds stress is the axial one. Furthermore, mixing is certainly not homogeneous, especially in the axial direction which is the direction of propagation of the shock waves. Nevertheless, mixing is assumed homogeneous along the transversal y direction. Averaged quantities $\overline{a}(x,t)$ are then performed along this direction

$$\overline{a}(x,t)=\frac{1}{N}\sum_{j=0}^{N-1} a(x,j\Delta y,t). \tag{9}$$

For incompressible flows, turbulent fluctuations a' of the quantity a are expressed as

$$a'(x,y,t)\equiv a(x,y,t)-\overline{a}(x,t).$$

On the other hand, for compressible flows, turbulent fluctuations a'' of the quantity a are expressed within the Favre averaging framework

$$a''(x,y,t)\equiv a(x,y,t)-\widetilde{a}(x,t),$$

where the mean velocity $\widetilde{a}(x,t)$ is given by

$$\widetilde{a}(x,t)\equiv\overline{\rho a}(x,t)/\overline{\rho}(x,t).$$

Figure 15 displays the turbulent kinetic energy profiles $\widetilde{K}=\widetilde{u_i''u_i''}/2$ at various times. We clearly see the strong generation of turbulent kinetic energy at the incident shock pas-

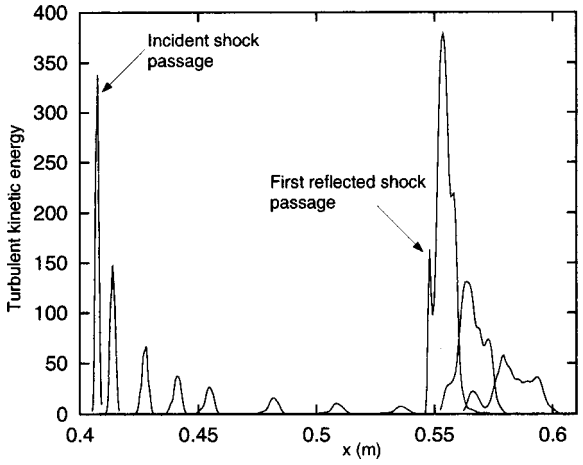

FIG. 15. Turbulent kinetic-energy profiles $\widetilde{K}=\widetilde{u_i''u_i''}/2$ at various times. We clearly see the strong generation of turbulent kinetic energy at the incident shock passage through the interface (first profile on the left side of the figure), and at the reshock (the third profile from the right side of the figure corresponds to the time when the reflected shock, which travels from right to left, is still interacting with the mixing zone).

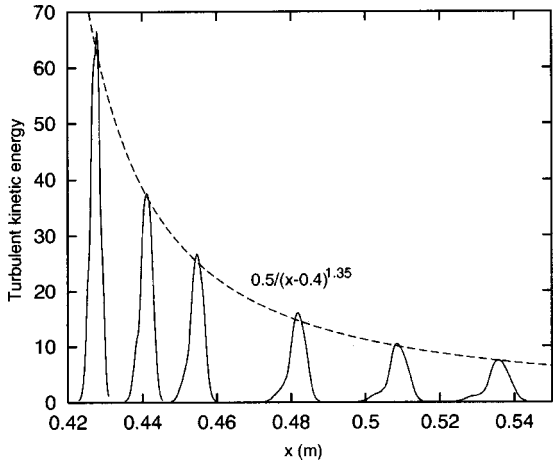

FIG. 16. Turbulent kinetic-energy profiles $\tilde{K}=\widetilde{u_i''u_i''}/2$ at various times after the incident shock–interface interaction and before the first reflected shock passage. The maximum amplitude of these profiles $\tilde{K}_{\max}$ decreases as the mixing zone moves in the shock tube and it follows a $(x-x_0)^{-1.35}$ power law, where $x_0=0.4$ is the initial position of the unperturbed interface.

sage through the interface and at the reshock. Figure 16 gives a zoom of the profiles before the reshock. The maximum amplitude of these profiles $\tilde{K}_{\max}$ decreases by diffusion and dissipation as the mixing zone moves in the shock tube and it follows a $(x-x_0)^{-1.35}$ power law, where $x_0=0.4$ is the initial position of the unperturbed interface in the simulations. As the mixing-zone averaged velocity is almost constant, we obtain: $\tilde{K}_{\max}(t)\,\alpha\, t^{-1.35}$. According to Kolmogorov,[36] the kinetic energy for freely evolving three-dimensional isotropic turbulence in incompressible fluids should decay as a power law $t^{-\alpha}$ where $\alpha=10/7$. On the bases of EDQNM calculations, Lesieur[37] found $\alpha=1.38$. From numerous results found in the literature and from their own grid turbulence experiments, Mohamed and Larue[38] show that the exponent in the decay power-law for the kinetic energy is equal to 1.3 and is independent of initial conditions such as Reynolds number, mesh size, solidity, and rod shape. We note that before the first reshock, the decay exponent $\alpha=1.35$ of the kinetic energy given by the 2D CADMÉE numerical simulations is close to all these values. However, since all the results cited concern the three-dimensional isotropic turbulence, we conclude that this is a pure coincidence. After the reshock, the kinetic-energy profiles are larger, (see Fig. 15), and it is no more easy to find a power-law behavior.

Figures 17(a) and 17(b) illustrate the anisotropy of the Reynolds stress tensor at the 125 mm abscissa and at the 169 mm abscissa, i.e., about 0.2 ms before and 0.3 ms after the interaction with the first reflected shock, respectively. Figure 17(c) gives the $\overline{u_1'u_1'}$ and $\overline{u_2'u_2'}$ profiles obtained from LDA experimental measurements at the 169 mm abscissa.[7] These figures clearly show the strong anisotropy of turbulence in the mixing zone: At the maximum of the profiles, the ratio $\overline{u_1'u_1'}/\overline{u_2'u_2'}$ reaches the value 3 in the experiments and about 2.5 in the calculations. Numerical values of the axial and radial components are twice greater than experimental measurements. However, experimental and numerical results may not be compared on a quantitative way because of the

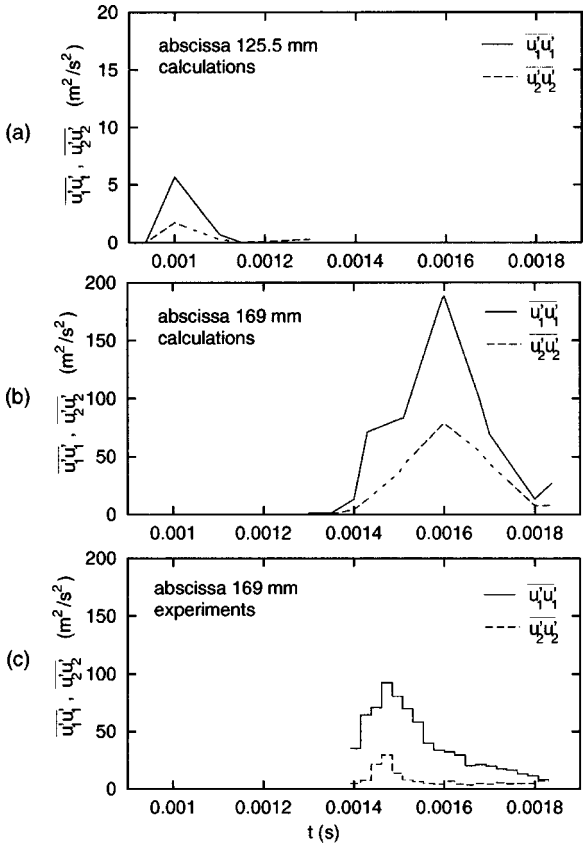

FIG. 17. Evolution of axial and radial components of the Reynolds stress tensor: (a) Numerical results at the 125 mm abscissa; (b) numerical results at the 169 mm abscissa ; (c) experimental data at the 125 mm abscissa.

2D character of the computations and it is well-known that the phenomenology of 2D turbulence is very different from the 3D one.

To determine the incompressible or compressible character of the fluctuations, we have calculated the turbulent Mach number, defined as $\sqrt{\tilde{K}}/c_s$ where c_s is the local sound speed. This Mach number is always less than few percents. Consequently, the fluctuations of the velocity field are quasi-incompressible. However, we do note that in the mixing zone the r.m.s. (root-mean-square) value of the density fluctuations $((\overline{\rho-\overline{\rho}})^2)^{1/2}/\overline{\rho}$ is about 0.4 after the incident shock passage and about 0.5 after the reshock.

We also calculated the turbulent kinetic-energy dissipation rate defined as $\overline{\rho}\tilde{\epsilon}=\overline{\sigma_{ij}\partial u_i''/\partial x_j}$. Figure 18 displays the profiles of the dissipation rate of turbulent kinetic energy at various times after the incident shock–interface interaction and before the first reshock. In Fig. 18, the maximum amplitude of these profiles $\tilde{\epsilon}_{\max}$ decreases as the mixing zone moves in the shock tube and it follows a $(x-x_0)^{-1.84}$ power law, where x_0 is the initial position of the unperturbed interface. As the mixing-zone averaged velocity is almost constant, we obtain: $\tilde{\epsilon}_{\max}(t)\alpha t^{-1.84}$. However, within the framework of a two-equation statistical model, the dissipation rate of the turbulent kinetic energy decreases as $d\tilde{K}/dt$, so, in this configuration, the dissipation rate should decrease as $(x-x_0)^{-2.35}$ or $t^{-2.35}$. This discrepancy can be explained by

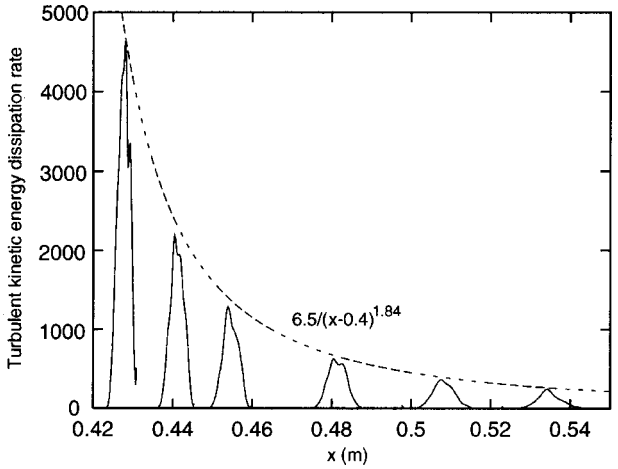

FIG. 18. Turbulent kinetic-energy dissipation rate profiles $\tilde{\epsilon}$ at various times after the incident shock–interface interaction. The maximum amplitude of these profiles $\tilde{\epsilon}_{\max}$ decreases as the mixing zone moves in the shock tube and it follows a $(x-x_0)^{-1.84}$ power law, where $x_0=0.4$ is the initial position of the unperturbed interface.

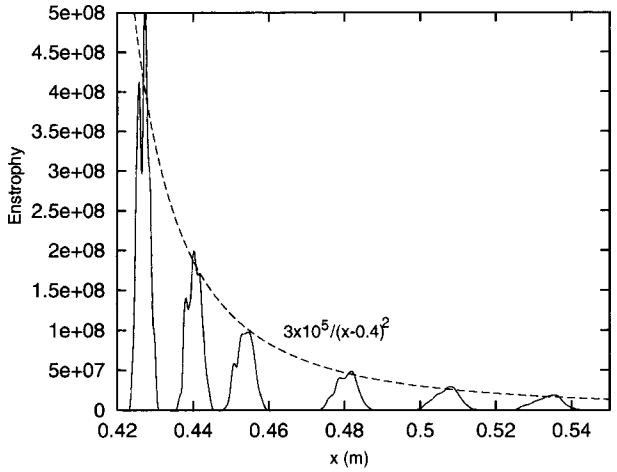

FIG. 19. Enstrophy profiles at various times after the incident shock–interface interaction. The maximum amplitude of these profiles $\Omega_{\max}$ decreases as the mixing zone moves in the shock tube and follows a $(x-x_0)^{-2}$ power law, where $x_0=0.4$ is the initial position of the unperturbed interface.

noticing that a turbulence created by a RM instability requires a certain amount of time to reach a perfect self-similar state. In other words, it requires a certain amount of time to reach an isotropic state with a spectral equilibrium. Moreover, the flow numerically simulated in this paper is a turbulence mixing and fluctuations of density, which are not taken into account in the turbulence model considered here, may alter the decay exponent. We also calculated the kinetic energy dissipation rate in the incompressible case, $\overline{\epsilon}=\nu(\partial u_i'/\partial x_j)(\partial u_i'/\partial x_j)$, and found profiles very similar to the compressible ones. This result is in agreement with the low values of the turbulent Mach number and proves that between interactions with the shock waves, the flow is quasi-incompressible.

D. The enstrophy behavior

The vorticity equation for a compressible viscous fluid is described by the Helmholtz equation

$$\frac{\partial}{\partial t}\boldsymbol{\omega}+\mathbf{u}.\nabla\boldsymbol{\omega}=-\boldsymbol{\omega}\nabla.\mathbf{u}+\boldsymbol{\omega}.\nabla\mathbf{u}-\frac{1}{\rho^2}\nabla p\times\nabla\rho+\nabla\times\left(\frac{1}{\rho}\nabla.\bar{\bar{\sigma}}\right). \tag{10}$$

In this equation, $\mathbf{u}$ is the velocity, $\boldsymbol{\omega}=\nabla\times\mathbf{u}$ the vorticity, $\nabla=(\partial/\partial x,\partial/\partial y,\partial/\partial z)$ the gradient operator and $\bar{\bar{\sigma}}$ the viscous shear stress tensor still defined in Eq. (2). The first and second terms on the right-hand-side of Eq. (10) represent the change of vorticity due to the compression and stretching of vortex lines, respectively. These two terms are linear in vorticity so that they would vanish in an irrotational flow. The third term on the right-hand-side, called the baroclinic term, may create vorticity in an initially irrotational flow. This term vanishes in a constant density incompressible fluid. The last term represents the change of vorticity by viscous effects and may be written as

$$\nabla\times\left(\frac{1}{\rho}\nabla.\bar{\bar{\sigma}}\right)=\mu\left[\frac{1}{\rho}\nabla^2\boldsymbol{\omega}-\frac{1}{\rho^2}\nabla\boldsymbol{\rho}\times\left(\nabla^2\mathbf{u}+\frac{1}{3}\nabla(\nabla.\mathbf{u})\right)\right]. \tag{11}$$

For a Newtonian incompressible fluid with constant kinematic viscosity coefficient $\nu=\mu/\rho$, this term reduces to the Laplacian of the vorticity $\nu\nabla^2\boldsymbol{\omega}$. In two-dimensional flow, the vorticity $\boldsymbol{\omega}$ is a vector perpendicular to the plane of the flow. The magnification of the vorticity by stretching of vortex lines, which is such an important feature of the inertial effect in three-dimensional turbulence, is consequently entirely absent in two-dimensional calculations. Finally, in a constant density incompressible fluid, Eq. (10) reduces to the well-known equation

$$\frac{\partial}{\partial t}\boldsymbol{\omega}+(\mathbf{u}.\nabla)\boldsymbol{\omega}=\nu\nabla^2\boldsymbol{\omega}. \tag{12}$$

In the 2D inviscid limit, the vorticity behaves as a pseudo-scalar conserved along the fluid trajectories. By taking the scalar product of $\boldsymbol{\omega}$ and Eq. (10) without the term of stretching of vortex lines (which is equal to zero in 2D-calculations), we obtain

$$\frac{\partial}{\partial t}\Omega+\mathbf{u}.\nabla\Omega=-2\Omega\nabla.\mathbf{u}-\frac{1}{\rho^2}\boldsymbol{\omega}.(\nabla p\times\nabla\rho)+\nu\boldsymbol{\omega}.\left[\nabla^2\boldsymbol{\omega}-\frac{1}{\rho}\nabla\rho\times\left(\nabla^2\mathbf{u}+\frac{1}{3}\nabla(\nabla.\mathbf{u})\right)\right]. \tag{13}$$

In this equation, Ω is the enstrophy density defined by $\Omega=\frac{1}{2}|\boldsymbol{\omega}|^2$. The second term on the left-hand-side and the three terms on the right-hand-side of Eq. (13) are called the advection, compression, baroclinic production, and dissipation terms, respectively. Figure 19 displays the averaged enstrophy profiles $\Omega(x)$ obtained by averaging the enstrophy along the transversal y direction, at various times after the incident shock–interface interaction and before the first reshock. In

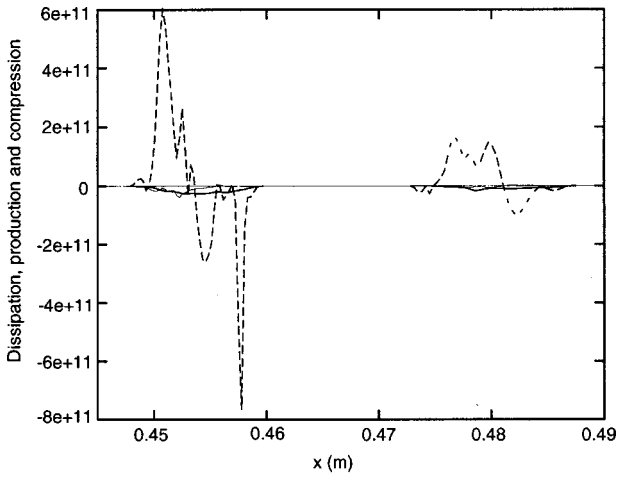

FIG. 20. Comparison of the profiles of the dissipation (thick full lines), baroclinic production (dotted lines) and compression terms (thin full lines) in the enstrophy budget at two instants after the incident shock–interface interaction.

Fig. 19, the maximum amplitude of these profiles $\Omega_{\max}$ decreases as the mixing zone moves in the shock tube and follows a $(x-x_0)^{-2}$ power law, where x_0 is the initial position of the unperturbed interface. As the mixing-zone averaged velocity is almost constant, we obtain $\Omega_{\max}(t)\alpha t^{-2}$. This time dependency of the mean-square vorticity is in agreement with the theoretical and numerical results of Batchelor in the context of a freely-decaying two-dimensional compressible turbulence.[33] In Eq. (13), the terms $(\nu\boldsymbol{\omega}).(\nabla^2\boldsymbol{\omega})$ and $(\nu\boldsymbol{\omega}).(-(1/\rho)\,\boldsymbol{\nabla}\rho\times(\nabla^2\mathbf{u}+(1/3)\boldsymbol{\nabla}(\boldsymbol{\nabla}.\mathbf{u})))$ represent the incompressible and compressible contributions to the enstrophy dissipation, respectively. After calculations of these contributions, we observed that the compressible part is at any time negligible towards the incompressible one. Figure 20 displays a comparison between various terms in the enstrophy budget at two instants after the incident shock–interface interaction. The profiles of dissipation, baroclinic production and compression show that the main contribution to the enstrophy budget comes from the baroclinic term. This result is in agreement with numerical simulations of two-dimensional homogeneous flows performed by Passot and Pouquet.[39] On the other hand, Kida and Orszag[40] showed that the main contributions to the enstrophy budget in three-dimensional flow come from the stretching and the dissipation terms, which give a positive and a negative contribution, respectively.

VI. CONCLUDING REMARKS

In this paper, we have presented the results of high-resolution 2D numerical simulations of shock-tube experiments of SF_6 incident on air performed by Poggi *et al.*[7,8] In these experiments, measurements demonstrate that the initial small scale perturbations of the interface develop into a turbulent mixing zone. The main result of this paper is to show that 2D calculations exhibit a turbulent regime compatible with the experimental data. In particular, we can see in numerical simulations the decay of the turbulence before the first reflected shock wave–turbulent mixing-zone interaction and its strong enhancement by reshocks. And finally, the mixing zone can be regarded as a region where large scales coexist with small scale turbulence more or less developed. So, we have compared our numerical results both with models for the nonlinear regime such as those proposed by Ramshaw[25] and Alon *et al.*,[26] and with statistical turbulence models, using the tools of fully developed turbulence, i.e., self-similar behavior, scaling laws and spectrum.

On one hand, after the incident shock passage and before the first reshock, large scales in the Richtmyer–Meshkov mixing fronts evolve versus time according to scaling laws given by models based on bubble-rise dynamics[26] ($t^{0.4}$ for the bubble fronts and $t^{0.66}$ for the spike fronts). These large scales of the motion govern the thickening of the mixing zone and retain memory of the initial conditions. In the literature, this dependence to the initial conditions has still been noticed in experiments, numerical simulations and models. In experiments,[4] the thin membrane which forms the initial interface has an influence on the initial growth rate of the mixing-zone thickness. In numerical simulations,[30] results slightly depend on the initial interface perturbations (amplitudes and wavelengths) and on the mesh size refinement. In models,[25] the kinetic energy deposited at the interface by the impulsive acceleration is a function of the initial conditions.

On the other hand, a statistical processing of the numerical results shows that the decay of the turbulent kinetic-energy scales as t^{α} with $\alpha=-1.35$ before the first reshock. However, the agreement with the value of the scaling law of the decaying of a free-evolving three-dimensional isotropic turbulence is certainly a pure coincidence. The enstrophy also decays as a power law t^{-2} that is in agreement with the theoretical and numerical results of Batchelor in the context of a freely-decaying two-dimensional incompressible turbulence,[33] although the flows simulated in this paper are bounded. Moreover, spectral analysis of the mixing layer exhibits a k^{-3} enstrophy cascade which is in agreement with theoretical studies of two-dimensional turbulence.[32,33] But some results moderate the conclusion that the flow is fully turbulent. We have seen that the turbulent kinetic-energy dissipation rate scales as $t^{-1.84}$ but in a fully 3D turbulent flow where dissipation plays an important role, we would have expected a $t^{\alpha-1}$ behavior where α is the exponent of the scaling law for the turbulent kinetic energy. However, we have to note that this agreement, using statistical turbulent models, does not take into account the density fluctuations. Moreover, let us recall that the theoretical scaling laws mentioned above give only an asymptotic limit in time and assume that the turbulence is homogeneous and isotropic, which is not true in our case. Indeed, measurement of the longitudinal and transversal velocity variances have proved that the flow is anisotropic in the mixing layer. Finally, before the first reshock, several quantities in the mixing zone adopt a quasi self-similar behavior even if the flow is not fully turbulent but still in a strongly nonlinear or weakly turbulent regime.

After the interaction between the first reflected shock wave with the mixing layer, the flow behavior is different.

Because of the 2D character of the simulations, large structures are still growing with time but power-law evolutions for various quantities (bubble and spike fronts, turbulent kinetic energy, enstrophy) are no more valid. This behavior may be explained by the presence of a weak turbulence far from equilibrium because the mixing layer has probably not evolved over a sufficiently long time between two reshocks to reach a spectral equilibrium.

Numerical simulations of these multimode Richtmyer–Meshkov experiments have also shown the influence of turbulent boundary layers on mean flow velocity measured in the middle of the tube. Indeed, turbulent boundary layers which develop on the shock-tube walls confine the flow and accelerate it. Furthermore, the lambda-shock structure observed in experiments is well reproduced by simulations.

Finally, numerical simulations presented in this paper allow us to characterize and better understand the flow in the Richtmyer–Meshkov instability induced mixing-zone. These 2D calculations have been done as a precursor to future three-dimensional simulations and the comparison between 2D and 3D results will permit to isolate effects that are due only to the 2D character, such as enstrophy cascade, or effects that are allowed by the third direction, such as vortex stretching.

ACKNOWLEDGMENTS

We thank O. Grégoire, F. Poggi, and D. Souffland for useful discussions.

[1] R. D. Richtmyer, ''Taylor instability in shock acceleration of compressible fluids,'' Commun. Pure Appl. Math. **13**, 297 (1960).
[2] E. E. Meshkov, ''Interface of two gases accelerated by a shock wave,'' Fluid Dyn. **4**, 101 (1969).
[3] S. G. Zaytsev, E. V. Lazareva, V. V. Chernukha, and V. M. Belyaev, ''Intensification of mixing at the interface between media of different densities upon the passage of a shock wave through it,'' Sov. Phys. Dokl. **30**, 579 (1985).
[4] M. Vetter and B. Sturtevant, ''Experiments on the Richtmyer–Meshkov instability of an air–SF_6 interface,'' Shock Waves **4**, 247 (1995).
[5] I. Galametz, ''Visualisation et mesure de masse volumique dans un mélange gazeux en tube à choc,'' thèse de l'Université de Lille (France), 1994; see also G. Rodriguez, I. Galametz, M.-H. Thorembey, C. Rayer and J.-F. Haas, *Visualization of shocked mixing zones using differential interferometry and X-rays, 20th ISSW, Pasadena (USA)*, edited by H. Hornung (World Scientific Press, Singapore, 1996).
[6] G. Jourdan, L. Houas, and M. Billiotte, ''Density evolution within a shock accelerated gaseous interface,'' Phys. Rev. Lett. **78**, 452 (1997).
[7] F. Poggi, ''Analyse par vélocimétrie d'un mélange gazeux créé par instabilité de Richtmyer–Meshkov,'' thèse de l'Université de Poitiers (France), 1997; see also F. Poggi, M.-H. Thorembey, J.-M. Koenig, G. Rodriguez, and J.-F. Haas, ''Measurements of velocity in the turbulent stage of gaseous mixtures induced by shock waves,'' Shock Waves (to be published).
[8] F. Poggi, M.-H. Thorembey, and G. Rodriguez, ''Velocity measurements in turbulent gaseous mixtures induced by Richtmyer–Meshkov instability,'' Phys. Fluids **10**, 2698 (1998).
[9] K. A. Meyer and P. J. Blewett, ''Numerical investigation of the stability of a shock-accelerated interface between two fluids,'' Phys. Fluids **15**, 753 (1972).
[10] L. D. Cloutman and M. F. Wehner, ''Numerical simulation of Richtmyer–Meshkov instabilities,'' Phys. Fluids A **4**, 1821 (1992).
[11] J. W. Grove, R. H. Holmes, D. H. Sharp, Y. Yang, and Q. Zhang, ''Quantitative theory of Richtmyer–Meshkov instability,'' Phys. Rev. Lett. **71**, 3473 (1993).
[12] R. H. Holmes, J. W. Grove, and D. H. Sharp, ''Numerical investigation of Richtmyer–Meshkov instability using front tracking,'' J. Fluid Mech. **301**, 51 (1995).
[13] R. M. Baltrusaitis, M. L. Gittings, R. P. Weaver, R. F. Benjamin, and J. M. Budzinski, ''Simulation of shock-generated instabilities,'' Phys. Fluids **8**, 2471 (1996).
[14] R. L. Holmes, G. Dimonte, B. Fryxell, M. L. Gittings, J. W. Grove, M. Schneider, D. H. Sharp, A. L. Velikovich, R. P. Weaver, and Q. Zhang, ''Richtmyer–Meshkov instability growth: experiment, simulation and theory,'' in Los Alamos National Laboratory, Report No. LA-UR-97-2606 (1997).
[15] C. Mügler and S. Gauthier, ''Numerical simulations of single-mode Richtmyer–Meshkov experiments,'' Phys. Rev. E **58**, 4548 (1998).
[16] S. Gauthier and M. Bonnet, ''A $k-\epsilon$ model for turbulent mixing in shock-tube flows induced by Rayleigh-Taylor instability,'' Phys. Fluids A **2**, 1685 (1990).
[17] F. L. Addesio, J. R. Baumgardner, J. K. Dukowicz, N. L. Johnson, B. A. Kashiva, R. M. Rauenzhan, and C. Zemach, ''CAVEAT : a computer code for fluid dynamics problems with large distortion and internal slip,'' in Los Alamos National Laboratory, Report No. 10613 (1990).
[18] J. O. Hirschfelder, C. F. Curtiss, and R. B. Bird, *Molecular theory of gases and liquids* (Wiley, New York, 1954).
[19] C. R. Wilke, ''A viscosity equation for gas mixtures,'' J. Chem. Phys. **18**, 517 (1950).
[20] E. A. Mason and S. C. Saxena, ''Approximate formula for the thermal conductivity of gas mixtures,'' Phys. Fluids **1**, 361 (1958).
[21] C. Mügler, L. Hallo, S. Gauthier, and S. Aubert, ''Validation of an ALE Godunov algorithm for solutions of the two-species Navier–Stokes equations,'' AIAA Pap. **96–2068**, (1996).
[22] J. K. Dukowicz, ''A general non-iterative Riemann solver for Godunov's method,'' J. Comput. Phys. **61**, 119 (1985).
[23] J. H. Williamson, ''Low-storage Runge-Kutta schemes,'' J. Comput. Phys. **35**, 48 (1980).
[24] B. Baldwin and H. Lomax, ''Thin layer approximation and algebraic model for separated turbulence flows,'' AIAA Pap. **78–257**, (1978).
[25] J. D. Ramshaw, ''Simple model for linear and nonlinear mixing at unstable fluid interfaces with variable acceleration,'' Phys. Rev. E **58**, 5834 (1998).
[26] U. Alon, J. Hecht, D. Ofer, and D. Shvarts, ''Power laws and Similarity of Rayleigh–Taylor and Richtmyer–Meshkov mixing fronts at all density ratios,'' Phys. Rev. Lett. **74**, 534 (1995).
[27] G. I. Barenblatt, in *Nonlinear Dynamics and Turbulence*, edited by G. I. Barenblatt, G. Ioss, and D. D. Joseph (Pitman, Boston, 1983), p. 48.
[28] C. Cherfils and A. K. Harrison, ''Comparison of different statistical models of turbulence by similarity methods,'' ASME Fluids Engineering Division Summer meeting, Nevada, June 19–23 1994.
[29] T. Pham and D. I. Meiron, ''A numerical study of Richtmyer–Meshkov instability in continuously stratified fluids,'' Phys. Fluids A **5**, 344 (1993).
[30] D. L. Youngs, ''Numerical simulation of mixing by Rayleigh–Taylor and Richtmyer–Meshkov instabilities,'' Laser Part. Beams **12**, 752 (1994).
[31] G. Dimonte and M. Schneider, ''Turbulent Richtmyer–Meshkov instability experiments with strong radiatively driven shocks,'' Phys. Plasmas **4**, 4347 (1997).
[32] R. H. Kraichnan, ''Inertial ranges in two-dimensional turbulence,'' Phys. Fluids **10**, 1417 (1967).
[33] G. K. Batchelor, ''Computation of the energy spectrum in homogeneous two-dimensional turbulence,'' Phys. Fluids Suppl. II **12**, 233 (1969).
[34] U. Frisch, *Turbulence, the legacy of A. N. Kolmogorov* (Cambridge University Press, Cambridge, 1995), pp. 241–243.
[35] J. C. McWilliams, ''The emergence of isolated coherent vortices in turbulent flow,'' J. Fluid Mech. **146**, 21 (1984).
[36] A. N. Kolmogorov, ''Decay of isotropic turbulence in incompressible viscous fluids,'' Dokl. Akad. Nauk SSSR **31**, 538 (1941).
[37] M. Lesieur, *Turbulence in Fluids*, 3rd revised and enlarged ed. (Kluwer Academic Publishers, Dordrecht, 1997).
[38] M. S. Mohamed and J. C. Larue, ''The decay power law in grid-generated turbulence,'' J. Fluid Mech. **219**, 195 (1990).
[39] T. Passot and A. Pouquet, ''Numerical simulations of compressible homogeneous flows in the turbulent regime,'' J. Fluid Mech. **181**, 441 (1987).
[40] S. Kida and S. A. Orszag, ''Enstrophy budget in decaying compressible turbulence,'' J. Sci. Comput. **5**, 1 (1990).